Journal of Power Sources 196 (2011) 659–665

Contents lists available at ScienceDirect

Journal of Power Sources

journal homepage: www.elsevier.com/locate/jpowsour

Proton exchange membrane fuel cells with nanoengineered AuPt catalysts at the cathode

Bin Fang, Bridgid N. Wanjala, Xiang Hu, Jordan Last, Rameshwori Loukrakpam, Jun Yin, Jin Luo, Chuan-Jian Zhong*

Department of Chemistry, State University of New York at Binghamton, 4400 Vestal Pkwy East, Binghamton, NY 13902, United States

ARTICLE INFO

Article history:
Received 25 May 2010
Received in revised form 20 July 2010
Accepted 24 July 2010
Available online 3 August 2010

Keywords:
PEM fuel cells
Gold–platinum nanoparticles
Bimetallic catalysts
Electrocatalysts
Phase properties

ABSTRACT

The report describes the findings of an investigation of nanoengineered gold–platinum (AuPt) catalysts in proton exchange membrane fuel cells. The membrane electrode assembly was prepared using carbon-supported Au_nPt_{100-n} nanoparticles with controlled sizes and bimetallic compositions that were thermally treated under controlled temperature, atmosphere, and time. Examples shown in this report included $Au_{22}Pt_{78}$/C and $Au_{49}Pt_{51}$/C catalysts treated at 400–500 °C. The electrocatalytic performances of these catalysts in the fuel cells was found to be dependent on the bimetallic composition and the nanoscale phase properties which are controlled by the thermal treatment parameters (temperature and time). Excellent fuel cell performance was observed for the catalysts which are characteristic of an alloyed AuPt phase with a lattice parameter approaching that for an Pt-rich alloy phase. The results have also demonstrated excellent stability of the nanoengineered AuPt catalysts in fuel cells. The observed combination of high activity and high durability of the selected AuPt catalysts indicated that this nanoengineered bimetallic catalyst system, upon further refinement and optimization of the nanoscale phase properties and durability serve as a promising candidate of electrocatalysts for the practical application in Proton Exchange Membrane fuel cells.

1. Introduction

The high conversion efficiency, low pollution, lightweight, and high power density of fuel cells such as proton exchange membrane fuel cell (PEMFC) are attractive because of a wide range of potential applications including their use as power sources in automobiles and space shuttles. However, one of the major challenges to the applications is the high overall manufacturing cost of PEMFCs, in which the cost of catalysts counts to 30% of the overall cost because currently platinum catalysts are required for both anodes and cathodes in the fuel cells [1,2]. The lowering of Pt loading in the catalysts, the improvement of the utilization of noble metals, and the increase of the stability of catalysts are some of the current approaches to reducing the high cost of catalysts for the ultimate commercialization of PEMFCs. The poor activity and poor durability of many existing Pt-based catalysts for the oxygen reduction reaction (ORR) in PEMFC's cathode are increasingly challenging problems. The reduction of platinum-loading in the membrane electrode assemblies (MEAs) while increasing the activity and stability has been a focus of fuel cell research [1]. Because the lowering of the cathode loadings to about 0.4 mg_{Pt} cm^{-2} is often limited by the poor activity of Pt for ORR, two important pathways of research interests in the past decade include optimization of electrode structures and implementation of more active Pt-alloy catalysts [1]. The development of Pt-based multimetallic or alloy electrocatalysts is currently one promising area of finding effective solutions to the problem [2,3]. In recent years, extensive studies of Pt-based alloy electrocatalysts have been based on measurements of rotating disc electrode methods, which have demonstrated the viability of bimetallic or trimetallic catalysts for increasing the electrocatalytic ORR activities [2–11]. However, the evaluation of the fuel cell performance of these catalysts has been rather limited [12–14]. The promising potentials of some of the nanoengineered catalysts in fuel cells have recently been demonstrated in our work. For example, carbon-supported trimetallic PtVFe nanoparticle catalysts prepared by our synthesis and processing methods were recently shown to exhibit enhanced electrocatalytic activity and stability in PEMFCs [15,16].

In this report, we describe findings of an investigation of the performance of nanoengineered bimetallic gold–platinum (AuPt) catalysts in PEMFCs. This bimetallic system is interesting because of the unique nanoscale size, composition, and phase properties which produce synergistic activity and stability, as demonstrated in our earlier work [8–11,17] and a number of recent reports

* Corresponding author. Tel.: +1 607 777 4605; fax: +1 607 777 4478.
E-mail address: cjzhong@binghamton.edu (C.-J. Zhong).

0378-7753/$ – see front matter © 2010 Elsevier B.V. All rights reserved.
doi:10.1016/j.jpowsour.2010.07.063

[7,12–14]. As reported in the recent work [7], the modification of Pt nanoparticles with Au clusters was shown to greatly stabilize the catalysts against dissolution under potential cycling regimes for oxygen reduction reaction. The examination of the viability of AuPt/C catalysts with different structures for ORR reaction and in fuel cells has attracted increasing interests in recent years, including alloyed [8,17], partially phase-segregated [9,10,17], and core-shell structured [11] catalysts. In a recent report [12], AuPt catalysts with a gold core and platinum shell structure were used as cathode catalysts and the test in single PEMFC cell showed promising application as an ultra-low Pt catalyst for fuel cells. Moreover, AuPt catalysts have also been studied in direct methanol fuel cells (DMFC) and fomic acid fuel cells. For example, the study of an AuPt catalyst with a 1:2 ratio in DMFC showed a peak power density of 120 mW cm^{-2}, which is higher than Pt catalyst (80 mW cm^{-2}) [13]. In another example, the study of AuPt nanoparticles with 1:1 atomic ratio supported on carbon powder prepared by co-reduction method showed about 35% higher power density than the cell with the Pt/C catalyst for formic acid oxidation reaction in a fuel cell [14]. Built upon our recent studies of the electrocatalytic activity of the nanostructured bimetallic AuPt catalysts for ORR and MOR (Methanol Oxidation Reaction) reactions [8–11,17], and the insight into the correlation of the electrocatalytic activity and stability of the bimetallic catalysts with a combination of electronic and geometric parameters such as lattice parameter, d-band vacancy, particle size, and surface structure [18–20], this work has focused on a detailed examination of the Au_nPt_{100-n}/C prepared by our nanoengineered synthesis and processing routes as cathode catalysts in PEM fuel cells. The nanoscale size, composition and phase properties of the bimetallic nanoparticles are shown to be quite promising in increasing both activity and stability of the cathode catalysts in PEM fuel cells.

2. Experimental

2.1. Chemicals

Decanethiol (DT, 96%), oleylamine (OAM, 70%) obtained from Aldrich, hydrogen tetrachloroaurate ($HAuCl_4$, 99%), tetraoctylammonium bromide (TOABr, 99%), hydrogen hexachloroplatinate (IV) ($H_2PtCl_6{\cdot}xH_2O$, 99.9%) obtained from Alfa Aesar, sodium borohydride ($NaBH_4$, 99%), methanol (99.9%), ethanol (99.9%), and Nafion (5 wt%) were purchased from Aldrich and used as received. Other chemicals included hexane (99.9%) and toluene (99.8%) from Fisher. Carbon Black (Vulcan XC-72) was obtained from Cabot. Water was purified with a Millipore Milli-Q water system

2.2. Synthesis of nanoparticles and catalysts

The synthesis and processing of Au_nPt_{100-n} nanoparticles and catalysts have been described in earlier reports [8–11,17]. The synthesis of AuPt nanoparticles involved a transfer of $AuCl_4^-$ and $PtCl_6^{2-}$ first from an aqueous solution of $HAuCl_4$ and H_2PtCl_6 into toluene solution using a phase transfer reagent (tetraoctylammonium bromide, TOABr) and a subsequent chemical reduction reaction. Thiols (e.g., decanethiol, DT) and amine compounds (e.g., oleylamine, OAM) were added to the organic solution as capping agents. An excess of aqueous $NaBH_4$ was slowly added for the reduction reaction. The resulting DT/OAM-encapsulated AuPt nanoparticles in toluene were collected by removing the solvent through evaporation in vacuo. The nanoparticle product was dispersed in hexane. The bimetallic composition of the AuPt nanoparticles was determined by DCP-AES. The control of AuPt composition in the desired proportion and high monodispersity (<±0.5 nm) was achieved by manipulating the precursor feed ratio. The protocol involved assembly of the as-synthesized nanoparticles on carbon support, followed by subsequent thermal treatment under controlled temperature and atmosphere. The thermal treatment involved heating the catalyst at 280 °C under 20% O_2 followed by treatment at 300–800 °C under 15% H_2. The actual loading ranged from 20 to 24% by mass for typical samples.

Glassy carbon (GC) disks (geometric area: 0.196 cm^2) were polished with 0.05 μm Al_2O_3 powders, followed by careful rinsing with deionized water. The geometric area of the GC electrode provides a measure of the loading of catalyst on the electrode surface used for the voltammetric characterization.

Nafion™ 212 membrane and Teflon™ treated Toray™ carbon paper were purchased from Electrochem Inc. 20% Pt/C catalyst was purchased from E-tek.

2.3. Instrumentation and measurements

The electrode was coated with the catalyst layer using modified method from a previous report [15,16]. Briefly, a typical suspension of the catalysts was prepared by suspending 1.0 mg catalysts (AuPt/C) in 1 mL Millipore water with diluted (5 vol.%) Nafion™ (5 wt%, Aldrich). The suspension was then quantitatively transferred to the surface of the polished GC disk. The electrodes were dried at room temperature. The electrochemical activity for oxygen reduction was measured using the hydrodynamic rotating disk electrode technique. The standard three-electrode configuration was used for the cell, and the reference and counter electrodes were in separate compartments of the electrochemical cell. Glassy carbon-based working electrode with a geometric surface area of 0.196 cm^2 was used, and 10 μL catalyst ink was pipetted and uniformly distributed over the glassy carbon surface. To prepare catalyst ink, 15 mg catalyst (Au_nPt_{100-n}/C) was added to a mixture of 12 mL of deionized water, 3 mL of isopropanol and 60 μL 0.25% Nafion solution, and sonicated for 10 min. The suspension was then quantitatively transferred to the surface of the polished GC disk. Cyclic voltammetry (CV) was performed at room temperature to clean the catalysts surface. Optimal grade sulfuric acid (Fisher Scientific) diluted with Milli-Q water to 0.5 M was used as electrolyte, and it was deaerated with high purity nitrogen before the measurement. The potentials were controlled with respect to the reference hydrogen electrode by a potentiostat from CH Instruments and reported with respect to reversible hydrogen electrode (RHE). The Rotating Disk Electrode (RDE) measurements were performed using a rotating disk electrode system made by Pine Instrument. Before the measurement, the sulfuric acid was saturated with pure oxygen. All measurements were performed under the rotating speed of 1600 rpm.

MEAs (5 cm^2 active area) used in this study were prepared by conventional catalyst coated substrate (CCS) method [15,16]. The electrocatalyst-Nafion ink was painted on a wet-proofed carbon paper (Toray™ EC-TP1-060T), using Au_nPt_{100-n}/C catalyst (20% metal loading, 0.4 mg_{Pt} cm^{-2}) for the cathode and Pt/C catalyst (20% Pt/C, E-tek, 0.4 mg_{Pt} cm^{-2}) for the anode. To enhance its adhesion to the Nafion 212 membrane, a thin coating of 5 wt% Nafion solution was painted onto the active side of the electrodes to produce a Nafion loading of ~0.4 mg cm^{-2}. For comparison, MEAs were also prepared using Pt/C (20% Pt/C, E-tek, 0.4 mg_{Pt} cm^{-2}) catalyst for both anode and cathode. The MEAs were prepared by hot pressing the sandwich structured Nafion™ 212 membrane (DuPont) and catalyst coated electrodes at 120 °C. The hot pressed MEAs were placed in a standard fuel cell test cell using gold-coated copper plates as current collector. The fuel cell was tested in a single-cell test station (Electrochem Inc.). The testing conditions included 100% humidified H_2 for the anode and 100% humidified O_2 for the cathode, each with a flow rate of 100 mL min^{-1}, a back pressure of

30 psi, and an operating temperature of 75 °C. The MEA was conditioned in the fuel cell for 1 h before recording the polarization curves. For each catalyst, we tested at least three MEAs to guarantee that our results were reproducible. In addition, we prepared MEAs with commercial Pt catalysts and compared the results as well, which further substantiated the validity of the MEAs prepared from our own catalysts [16].

Other analytical techniques were also used for the characterization of the nanoparticles and catalysts. Transmission electron microscopy (TEM) was performed on Hitachi H-7000 electron microscope (100 kV). For TEM measurements, the catalyst samples were suspended in hexane solution and were drop cast onto a carbon-coated copper grid followed by solvent evaporation in air at room temperature.

The composition was analyzed using the direct current plasma-atomic emission spectroscopy, which was performed using an ARL Fisons SS-7 direct current plasma-atomic emission spectrometer (DCP-AES). The measurements were made on emission peaks at 267.59 and 265.95 nm for Au and Pt, respectively. The nanoparticle samples were dissolved in concentrated aqua regia, and then diluted to concentrations in the range of 1–50 ppm for analysis. Calibration curves were made from dissolved standards with concentrations from 0 to 50 ppm in the same acid matrix as the unknowns. Standards and unknowns were analyzed 10 times each for 3 second counts. Instrument reproducibility, for concentrations greater than 100 times the detection limit, results in <±2% error. Inductively coupled plasma mass spectrometry (ICP-MS) method was also used for the composition analysis, which confirmed the results obtained by the DCP-AES method.

Thermogravimetric analysis (TGA) was performed on a Perkin-Elmer Pyris 1-TGA for determining the metal loading of the carbon-supported catalysts. Typical samples weighed 4 mg and were heated in a platinum pan under 20% O_2 at a rate of 10 °C min^{-1}.

3. Results and discussion

The detailed characterization of the as-synthesized AuPt nanoparticles with controllable size and composition and the AuPt/C catalysts of different compositions have been described in recent reports [8–11]. Table 1 summarizes the composition, size, and phase properties the Au_nPt_{100-n}/C catalysts described in this work. In addition to some differences in particle sizes, there are subtle differences in nanoscale alloying or partial phase segregation for these bimetallic nanoparticles [9,10,17]. The alloying and phase segregation properties of different Au_nPt_{100-n}/C catalysts were determined by XRD analysis [8–11,17], from which the lattice parameter (a) and relative weight (%) of different phases were derived by spectral deconvolution [17]. The results were compared with the lattice parameters for pure Au and pure Pt nanoparticle catalysts, 0.4075 and 0.3915 nm, respectively.

As shown by the lattice parameters and their corresponding relative weight of the identified phase in the bimetallic nanoparticles [17], the lattice parameter and their relative percentages indicates the following characteristics: (1) Catalyst-A consists of partially phase-segregated Au and partially alloyed phases; (2) Catalyst-B is largely in an alloyed phase for 400 °C and contains a partially phase-segregated Au phase and a partially alloyed phase that approaches a Pt-rich phase for 500 °C; and (3) Catalyst-C also consists of a partially phase-segregated Au phase and a partially alloyed phase that is predominated by a Pt-rich phase.

The study of the fuel cell performance of Catalyst-A ($Au_{22}Pt_{78}$/C), Catalyst-B ($Au_{22}Pt_{78}$/C), and Catalyst-C ($Au_{49}Pt_{51}$/C) showed that the electrocatalytic activity of the AuPt/C catalysts was highly dependent on the size, composition, surface and phase properties.

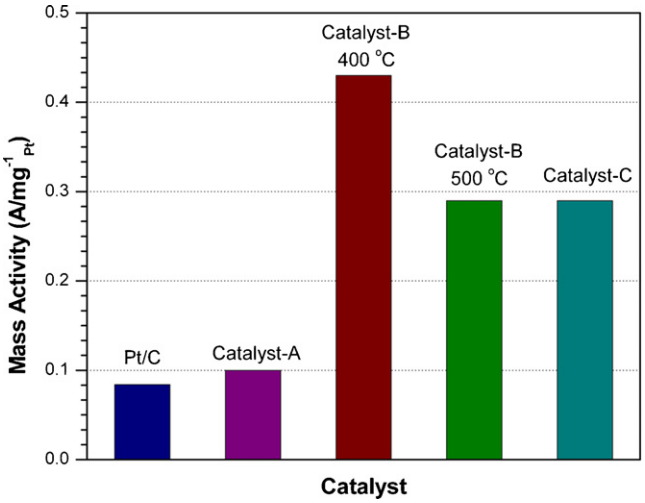

Fig. 1. Mass activity of different catalysts obtained from RDE measurements for ORR using different catalysts Pt/C, $Au_{22}Pt_{78}$/C and $Au_{49}Pt_{51}$ on glassy carbon electrode (loading 10 μg, 0.196 cm^2) in 0.5 M H_2SO_4. Scan rate: 10 mV s^{-1}, and rotating speed: 1600 rpm (E = 0.858 V vs. RHE).

The thermal treatment involved heating from room temperature to 280 °C under 20% O_2 for 60 min (Catalyst-A) and 30 min (Catalyst-B) before further treatment at 300–800 °C under 15% H_2 for 2 hrs. Catalysts with two different compositions, i.e., $Au_{22}Pt_{78}$/C (Catalyst-B 500 °C) and $Au_{49}Pt_{51}$/C (Catalyst-C) were prepared under the same thermal treatment conditions.

The Pt-mass activities of these catalysts for ORR were compared first based on the kinetics currents at 0.858 V (vs. RHE) obtained from measurements of RDE curves. Fig. 1 shows a representative set of mass activity data comparing the activities for Pt/C, $Au_{22}Pt_{78}$/C and $Au_{49}Pt_{51}$/C catalysts in 0.5 M H_2SO_4 electrolyte.

For Catalyst-A ($Au_{22}Pt_{78}$), the Pt-mass activity is 0.10 A $mg^{-1}{}_{Pt}$, which is almost the same as the Pt/C catalyst (0.084 A $mg^{-1}{}_{Pt}$) under the same condition. For Catalyst-B $Au_{22}Pt_{78}$, the Pt-mass activity is 0.43 A $mg^{-1}{}_{Pt}$ for 400 °C and 0.29 A $mg^{-1}{}_{Pt}$ for 500 °C, which are 3 ~ 5 times larger than that for Pt/C. For Catalyst-C ($Au_{49}Pt_{51}$/C), the Pt-mass activity of 0.29 A $mg^{-1}{}_{Pt}$, which is ~3 times greater than that for Pt/C. These subtle differences reflected the effects of a combination of composition and thermal treatment conditions of the catalysts on the ORR activities, which are based on the RDE measurements. In the following two subsections, the results are compared for the catalysts with different thermal treatment conditions and different compositions, respectively.

The hydrogen adsorption/desorption characteristics were obtained with glassy carbon electrode inked with the catalyst using CV technique, which provided a measure of the electrochemical active area (ECA) of the catalysts. The potential was cycled between 0.02 and 1.15 V (vs. RHE) at 50 mV s^{-1} in a solution of 0.5 M H_2SO_4 purged with nitrogen at 25 °C. Fig. 2 shows a representative set of CV data, which are characteristic of the surface adsorption/desorption of hydrogen and Oxidation for Pt/C and AuPt/C catalysts. The CV curves exhibit well-defined hydrogen adsorption/desorption peaks in the potential region of 0–0.4 V and adsorption/desorption peaks for surface oxide species from 0.7 to 1.0 V. In comparison with those observed for Pt/C, the voltammetric waves observed for AuPt/C catalysts are apparently larger in the hydrogen adsorption/desorption potential region. Catalyst-B (400 °C) exhibited the largest ECA value. The origin of the large ECA values is not completely clear [17], but it could be related to the rough or porous surface properties of the catalysts which is subject to further investigation.

Table 1
Summary of the composition, size, and phase properties of the AuPt/C catalysts described in this report.

Catalyst	Composition	Thermal treatment temp. (°C)	Treatment condition (20%O_2)	Particle size (nm)	Lattice parameter (a) and relative % based on XRD[6,7,9,17] (a (Au) = 0.4075 nm, a (Pt) = 0.3915 nm)
A	$Au_{22}Pt_{78}$/C	500	60 min	4.5 ± 0.8	a (Au) = 0.4087 nm(43%), a (AuPt) = 0.4030 nm (57%)
B	$Au_{22}Pt_{78}$/C	400	30 min	6.9 ± 1.1	a (Au) = 0.4014 nm(34%) a (AuPt) = 0.4014 nm (66%)
B	$Au_{22}Pt_{78}$/C	500	30 min	5.6 ± 0.8	a (Au) = 0.4058 nm(68%) a (AuPt) = 0.3973 nm (32%)
C	$Au_{49}Pt_{51}$/C	500	30 min	7.5 ± 1.7	a (Au) = 0.4095 nm(10%) a (AuPt) = 0.4003 nm (90%)

3.1. Comparison of catalysts with different thermal treatment conditions

Fig. 3 shows a representative set of fuel cell performance data (at 75 °C) comparing Catalyst-A and -B with the same composition ($Au_{22}Pt_{78}$/C) with Pt/C catalyst. The comparison was under the condition of 0.4 mg_{Pt} cm^{-2} for each catalyst. Note that the fuel cells with different cathode catalysts showed similar open circuit potential. The current (I)–voltage (V) curve characteristics in three regions were examined, including Region I: activation polarization region, Region II: Ohmic polarization region, and Region III: concentration polarization region. The data were compared in terms of polarization curve (i.e., I–V curve) and power density (P) curve (i.e., I–P curve) in these three regions.

In Region I, which mainly reflects the reaction rate loss, the fuel cells with both Catalyst-A and -B treated at 400 and 500 °C showed almost identical performance in the I–P curve. However, there is a subtle difference in the I–V curve. Both Catalyst-A and -B are clearly better than the commercial Pt/C catalyst, and Catalyst-B is better than Catalyst-A, which is consistent with the mass activity data shown in Fig. 1. For Catalyst-B, a close examination shows that the voltage drop for the 500 °C treated catalyst is apparently less pronounced than that for the 400 °C treated one, suggesting that the 500 °C treated catalyst is better than the 400 °C treated catalyst. This finding appears to be the opposite of the mass activity data as shown in Fig. 1, indicating that the performance of a catalyst in an actual fuel cell cannot solely be based on the mass activity data obtained from RDE measurements.

In Region III, which mainly reflects mass transport losses due to concentration polarization, the performance of Catalyst-B (treated at both 400 and 500 °C) was found to be better than the commercial Pt/C catalyst, in agreement with the mass activity data (see Fig. 1). In contrast, Catalyst-A showed much poorer performance than the commercial Pt/C catalyst, which was apparently not completely consistent with the fact that both had similar mass activities as shown in Fig. 1. Interestingly, the finding that the fuel cell with the 500 °C treated catalyst showed poorer performance than that with the 400 °C treated catalyst in Region III is clearly the opposite of the performance order in Region I. For the data in Fig. 3, there are in fact two types of behavior. One is the type expected for the well-defined three regions, as observed for catalysts Pt and B (400 °C). We believe that this type represents largely the true behavior of the catalysts. The other type is the poorly defined three regions as represented by catalysts A and B (500 °C), which cannot represent the true behavior of the catalysts.

Part of the origin of the poorer fuel cell performance for these catalysts is believed to be associated with effects of mass transport and water flooding in the catalyst layer of the fuel cell. For example, the steeper potential drop in the I–V curve for Catalyst-A than

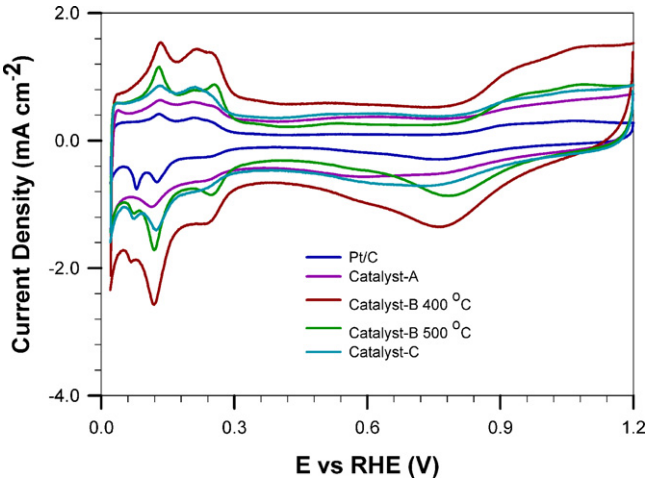

Fig. 2. Cyclic voltammetric curves for Pt/C and AuPt/C catalysts on a GC electrode in 0.5 M H_2SO_4 electrolyte saturated with N_2. Scan rate: 50 mV s^{-1}.

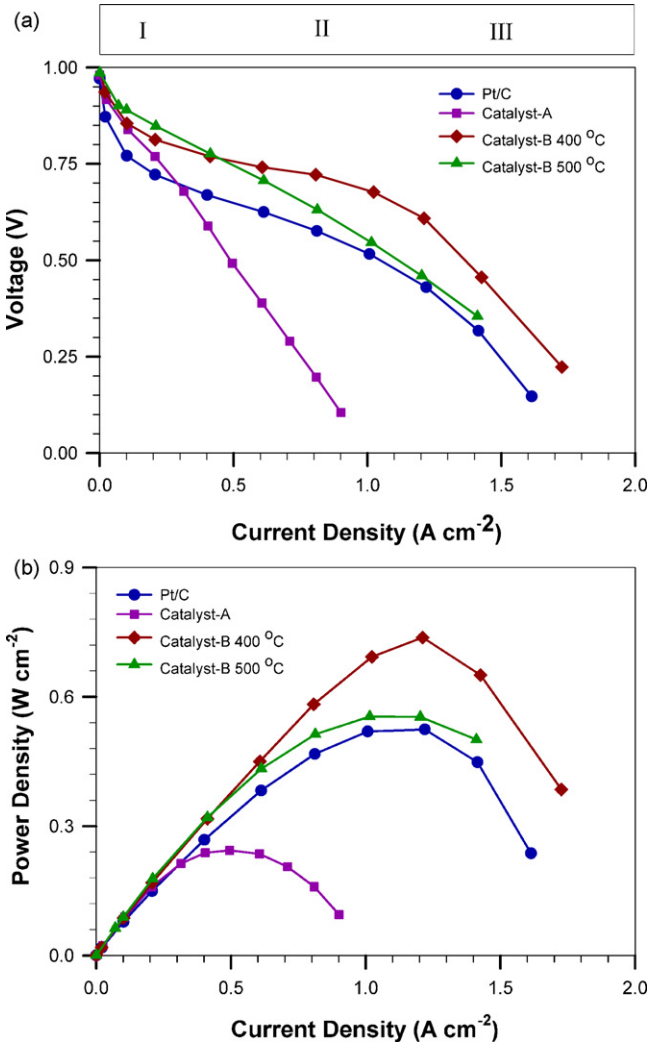

Fig. 3. I–V (a) and I–P (b) curves for PEMFCs with different cathode catalysts: Pt/C, Catalyst-A ($Au_{22}Pt_{78}$/C 500 °C), and Catalyst-B ($Au_{22}Pt_{78}$/C 400 °C and 500 °C) at 75 °C (H_2/O_2, back pressure 30 psi). Pt loading in both anode and cathode was 0.4 mg_{Pt} cm^{-2} for all MEAs.

the other catalysts is believed to partially reflect the gas transport being blocked by water flooding in the fuel cell. The water flooding could have blocked the porous structures in the catalyst layer, and thus build a barrier to the gas transport in the catalyst layer. In the case of the observed reversal of performance between the 400 and 500 °C treated catalysts (Catalyst-B) from Region I to Region III, it could be due to water flooding in the catalyst layer as a result of the higher current density in Region III than in Region I. Among different possibilities contributing to water flooding, the effect of thermal treatment temperature on the surface hydrophobicity of the catalyst is considered to be an important factor for regulating the water flooding in the catalyst layer. A higher temperature could lead to an enhanced burning or effective removal of surface carbons or carbon residues around the nanoparticles supported on carbon, thus rendering the catalyst a less hydrophobic microenvironment. The detailed understanding of such microenvironment structures is still part of our on-going investigation. In a preliminary examination of the hydrophobicity properties, the data from contact angle measurement showed AuPt/C catalysts were more hydrophobic than the commercial catalyst. The presence of possible pore structure for the various catalysts using additional techniques such as Barrett–Joyner–Halenda (BJH) or Molecularly imprinted polymers (MIP) methods would be needed for explaining the different mass transport performance.

In the Ohmic polarization region (Region II), there is a possibility of resistance change of the catalyst layer partly associated with water flooding as a result of the increase in current density. For example, the fuel cell with Catalyst-A showed a very low current density (e.g., 0.3 A cm^{-2} at 0.65 V), whereas the fuel cell with Catalyst-B showed much higher current density (e.g., 1.1 A cm^{-2} at 0.65 V) than that Pt/C catalyst (e.g., 0.5 A cm^{-2} at 0.65 V). It is possible that the water flooding in Catalyst-A layer increased the overall electronic resistance.

In Fig. 3(b), the peak power density values determined from the *I–P* curves of the fuel cells with different cathode catalysts provide useful information for further assessing the overall performance of the catalysts in the fuel cell. In comparison with the use of Pt/C as cathode catalyst, which showed a peak power density of 0.52 W cm^{-2}, the poor-performance of Catalyst-A showed a significantly reduced peak power density (0.24 W cm^{-2}). In contrast, the performance-enhanced fuel cells with Catalyst-B showed increased peak power densities, 0.74 W cm^{-2} for 400 °C and 0.56 W cm^{-2} for 500 °C. Note that the power density difference reflects differences in fuel cell characteristics in the mass transport region (i.e., the potential difference at large current density). The different mass transport loss could be a result of the different roughness or pore structures of the catalysts, which is qualitatively supported by the ECA data described earlier. It is evident that a combination of both the thermal treatment time and temperature must have played an important role in dictating the fuel cell performance of the catalysts.

3.2. Comparison of catalysts with different composition

Fig. 4 shows a representative set of *I–V* and *I–P* curves to compare catalysts with two different composition, Catalyst-B ($Au_{22}Pt_{78}$/C) and Catalyst-C ($Au_{49}Pt_{51}$/C), both of which were treated at 500 °C. Again, similar to the above comparison of $Au_{22}Pt_{78}$/C catalysts with different thermal treatment conditions, the examination of the *I–V* curves in the three Regions provides useful information for assessing the composition effect of the catalysts on the fuel cell performance.

The fuel cells with $Au_{22}Pt_{78}$/C and $Au_{49}Pt_{51}$/C catalysts seem to show a comparable performance in Region I, though $Au_{22}Pt_{78}$/C exhibited a slightly better performance than the $Au_{49}Pt_{51}$/C catalyst. This finding is largely consistent with the mass activity data

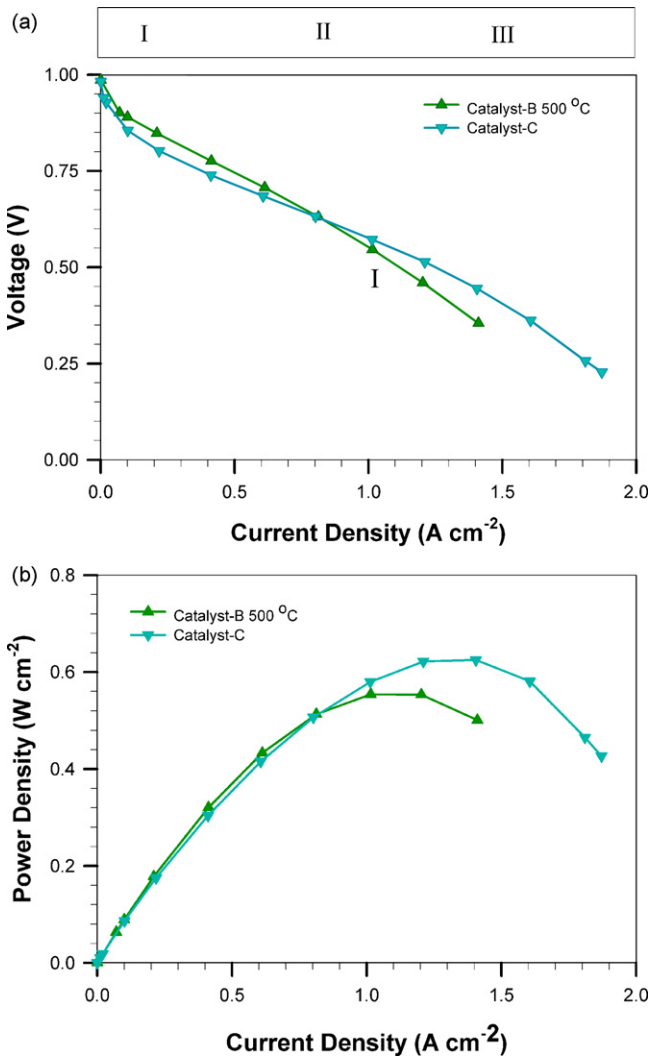

Fig. 4. *I–V* (a) and *I–P* (b) curves for PEMFCs with different cathode catalysts: Catalyst-B ($Au_{22}Pt_{78}$/C, 500 °C), and Catalyst-C ($Au_{49}Pt_{51}$/C, 500 °C) at 75 °C (H_2/O_2, back pressure 30 psi). Pt loading in both anode and cathode was 0.4 mg_{Pt} cm^{-2} for all MEAs.

determined from the RDE measurements as shown in Fig. 1, where these two catalysts showed almost identical mass activities.

In Region III, the slope for the potential drop for the fuel cell with $Au_{49}Pt_{51}$/C catalyst was found to be smaller than that of the 500 °C treated $Au_{22}Pt_{78}$/C catalyst. There is apparently a reversal of the relative cell voltages in the *I–V* curve between these two catalysts from Regions I to -III. This characteristic is believed to reflect the composition and phase effects on the catalytic activity [17]. The surface hydrophobicity of the $Au_{49}Pt_{51}$/C catalyst layer (20% metal loading, 0.4 mg_{Pt} cm^{-2}) could be different from that for the $Au_{22}Pt_{78}$/C catalyst. A slightly higher degree of hydrophobicity could have enabled a more hydrophobic microenvironment to facilitate the release of water produced by the fuel cell. This enhanced improvement in the gas transport could be partially responsible for the enhanced performance of $Au_{49}Pt_{51}$/C over $Au_{22}Pt_{78}$/C.

In Region II, the fuel cell with 500 °C treated $Au_{22}Pt_{78}$/C catalyst showed a higher potential than the one with the $Au_{49}Pt_{51}$/C catalyst. For example, the fuel cell with $Au_{49}Pt_{51}$/C showed a current density of 0.7 A cm^{-2} at 0.65 V, which is lower than that for $Au_{22}Pt_{78}$/C (1.1 A cm^{-2}). However, this difference was reversed in Region III likely due to a contribution of water flooding at the high current density to the overall resistance of the catalyst layer.

Table 2
Summary of electrocatalytic mass activity and fuel cell performance data for the different catalysts.

Catalyst	Electrochemical area ($m^2\ g^{-1}_{Pt}$)	Mass activity ($A\ mg^{-1}_{Pt}$)	Specific activity ($mA\ cm^{-2}$)	I (FC) @0.65 V ($A\ cm^{-2}$)
Pt/C (commercial catalyst)	66	0.084	0.13	0.5
$Au_{22}Pt_{78}$/C (A) 500 °C	85	0.10	0.12	0.3
$Au_{22}Pt_{78}$/C (B) 400 °C	278	0.43	0.15	1.1
$Au_{22}Pt_{78}$/C (B) 500 °C	197	0.29	0.15	0.8
$Au_{49}Pt_{51}$/C (C) 500 °C	213	0.29	0.14	0.7

In Fig. 4b, the comparison of the *I–P* curves between the catalysts of the two different compositions provides a further confirmation of the above conclusion. The fuel cell performance with the $Au_{49}Pt_{51}$/C catalyst, which has a peak power density of 0.64 W cm^{-2}, is better than that of the $Au_{22}Pt_{78}$/C catalyst (0.56 W cm^{-2}).

3.3. Assessment of activity and stability

Table 2 summarizes the results for the electrocatalytic activity data obtained from CV, RDE measurements and the fuel cell performance data obtained from the measurements of *I–V* and *I–P* curves for MEAs with different AuPt/C catalysts in the PEM fuel cells.

It is evident that the 400 °C treated Catalyst-B ($Au_{22}Pt_{78}$/C) exhibited the best performance among the catalysts examined in terms of mass activity and fuel cell characteristics. In comparison with our previous reports on the performance of PtVFe catalyst in PEMFC at the same conditions (the mass activity ~0.30 A mg^{-1}_{Pt}, and the peak power density is ~0.8 W cm^{-2}) [15], the AuPt catalyst showed an enhanced mass activity and comparable peak power density.

It is believed that the unique phase properties of the AuPt catalysts [17] must have played an important role in regulating the mass activity and the fuel cell performance of the catalysts. As shown in Table 1 for Catalyst-A, the catalyst consists of partially phase-segregated Au and partially alloyed phases. For Catalyst-B, the 400 °C treated catalyst is largely in an alloyed phase, whereas the 500 °C treated one consists of a partially phase-segregated Au phase and a partially alloyed phase that approaches a Pt-rich phase. For Catalyst-C, the catalyst also consists of a partially phase-segregated Au phase and a partially alloyed phase that is predominated by a Pt-rich phase. Therefore, the observed optimal fuel cell performance can be partly attributed to the alloyed AuPt phase with a lattice parameter approaching that for a Pt-rich phase.

The catalyst stability (or durability) is another important parameter for the assessment of the overall fuel cell performance of the catalysts, which was examined by measuring the cell voltage vs. time at an intermediate current density. Fig. 5 shows a typical set of fuel cell durability data for a PEMFC with Catalyst-B ($Au_{22}Pt_{78}$/C) as the cathode catalyst. The measurements were carried out under a current density of 0.8 A cm^{-2} (catalyst-B 400 °C) and 0.6 A cm^{-2} (Catalyst-B 500 °C) over a period of 10 days.

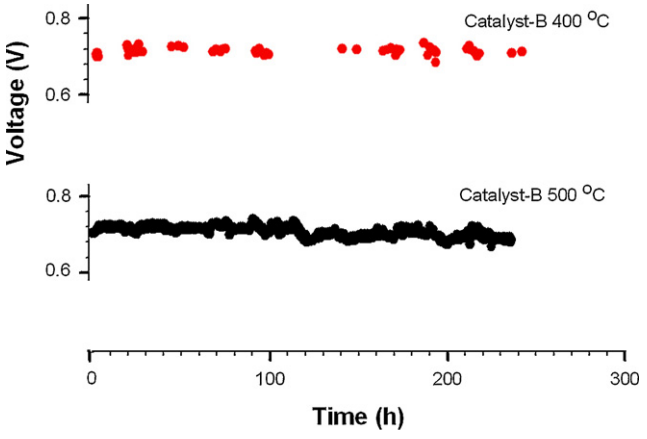

Fig. 5. Cell voltage under a controlled current density (0.8 A cm^{-2}) (for Catalyst-B (400 °C)) and 0.6 A cm^{-2} (for Catalyst-B (500 °C)) as a function of time for assessing the stability of the catalysts in PEMFCs at 75 °C (H_2/O_2, back pressure 30 psi). Pt loading in both anode and cathode was 0.4 mg_{Pt} cm^{-2} for all MEAs.

It is evident that the cell voltages for the fuel cells using catalyst-B as the cathode catalyst were practically unchanged over the 10-day testing period. There was no indication of a significant decrease in cell voltage and power density. The preliminary durability test result provided a rough idea about the catalyst stability, but a more realistic test should use voltage cycling method. The cell voltage measurements for an even longer period of time and accelerated tests wherein the voltage is cycled between 0.6 and 0.925 V are in progress for a comprehensive assessment of the catalyst durability in fuel cells.

4. Conclusion

In summary, the nanoengineered Au_nPt_{100-n}/C catalysts with different compositions and different thermal treatment parameters have been examined in PEM fuel cells. The catalysts have been shown to exhibit different electrocatalytic performances in the fuel cells depending on the bimetallic composition and the phase properties, the latter of which were controlled by the thermal treatment conditions. The observed enhancement in fuel cell performance is partly attributed to the alloyed AuPt phase with a lattice parameter approaching that for a Pt-rich phase. The catalysts have also been demonstrated to exhibit excellent stability in fuel cells, which reflects the synergistic effect of the nanoscale bimetallic alloying character on the catalyst activity. The enhanced performance of the AuPt/C catalysts in both activity and stability indicate that the nanoengineered bimetallic catalysts serve as a promising candidate for practical applications in fuel cells.

Acknowledgements

The research work was supported by the National Science Foundation (CBET-0709113), and in part by NYSTAR (C060057) and DoE SBIR (DE-FG02-07ER84843). The authors wish to thank Bill Brinkerman and George Shovlowsky for assistance in laboratory hardware work.

References

[1] H.A. Gasteiger, S.S. Kocha, B. Sompalli, F.T. Wagner, Appl. Catal. B: Environ. 56 (2005) 9–35.
[2] C.J. Zhong, J. Luo, B. Fang, B.N. Wanjala, P.N. Njoki, R. Loukrakpam, J. Yin, Nanotechnology 21 (2010) 062001.
[3] C.J. Zhong, J. Luo, P. Njoki, D. Mott, B. Wanjala, R. Loukrakpam, S. Lim, L. Wang, B. Fang, Z. Xu, Energy Environ. Sci. 1 (2008) 454–466.
[4] L. Xiong, K.L. More, T. He, J. Power Sources 195 (2010) 2570–2578.
[5] I. Takahashi, S.S. Kocha, J. Power Sources 195 (2010) 6312–6322.
[6] S.C. Zignani, E. Antolini, E.R. Gonzalez, J. Power Sources 191 (2009) 344–350.
[7] J. Zhang, K. Sasaki, E. Sutter, R.R. Adzic, Science 315 (2007) 220–222.
[8] J. Luo, P. Njoki, Y. Lin, L. Wang, D. Mott, C.J. Zhong, Electrochem. Commun. 8 (2006) 581–587.
[9] J. Luo, M.M. Maye, V. Petkov, N.N. Kariuki, L. Wang, P. Njoki, D. Mott, Y. Lin, C.J. Zhong, Chem. Mater. 17 (2005) 3086–3091.

[10] D. Mott, J. Luo, A. Smith, L. Wang, P.N. Njoki, C.J. Zhong, Nanoscale Res. Lett. 2 (2007) 12–16.
[11] J. Luo, L.Y. Wang, D. Mott, P. Njoki, Y. Lin, T. He, Z. Xu, B. Wanjala, S. I-Im Lim, C.J. Zhong, Adv. Mater. 20 (2008) 4342–4347.
[12] Y. Ma, H. Zhang, H. Zhong, T. Xu, H. Jin, X. Geng, Catal. Commun. 11 (2010) 434–437.
[13] G. Selvarani, S.V. Selvaganesh, S. Krishnamurthy, et al., J. Phys. Chem. C 113 (2009) 7461–7468.
[14] J. Xu, T. Zhao, Z. Liang, J. Power Sources 185 (2008) 857–861.
[15] B. Fang, J. Luo, P.N. Njoki, R. Loukrakpam, D. Mott, B. Wanjala, X. Hu, C.J. Zhong, Electrochem. Commun. 11 (2009) 1139–1141.
[16] B. Fang, J. Luo, P.N. Njoki, R. Loukrakpam, D. Mott, B. Wanjala, X. Hu, C.J. Zhong, Electrochim. Acta (2010), doi:10.1016/j.electacta.2010.02.048.
[17] B.N. Wanjala, J. Luo, R. Loukrakpam, B. Fang, D. Mott, P.N. Njoki, M. Engelhard, H.R. Naslund, J.K. Wu, L. Wang, O. Malis, C.J. Zhong, Chem. Mater. 22 (2010) 4282–4294.
[18] L. Xiao, L. Zhuang, Y. Liu, J.T. Lu, H.D. Abruna, J. Am. Chem. Soc. 131 (2009) 602–608.
[19] C.W.B. Bezerra, L. Zhang, H. Liu, K. Lee, A.L.B. Marques, E.P. Marques, H. Wang, J. Zhang, J. Power Sources 173 (2007) 891–908.
[20] S.H. Joo, K. Kwon, D.J. You, C. Pak, H. Chang, J.M. Kim, Electrochim. Acta 54 (2009) 5746–5753.